Journal of Power Sources 270 (2014) 457–467

Contents lists available at ScienceDirect

Journal of Power Sources

journal homepage: www.elsevier.com/locate/jpowsour

Highly active $La_{0.4}Sr_{0.6}Co_{0.8}Fe_{0.2}O_{3-\delta}$ nanocatalyst for oxygen reduction in intermediate temperature-solid oxide fuel cells

Corina M. Chanquía [a, b, c, *], Liliana Mogni [a, b, c], Horacio E. Troiani [a, b, c], Alberto Caneiro [a, b, c]

[a] Centro Atómico Bariloche-Comisión Nacional de Energía Atómica (CAB-CNEA), Av. Ezequiel Bustillo 9500, R8402AGP San Carlos de Bariloche, Río Negro, Argentina
[b] Consejo Nacional de Investigaciones Científicas y Técnicas (CONICET), Avenida Rivadavia 1917, C1033AAJ Buenos Aires, Argentina
[c] Instituto Balseiro, Universidad Nacional de Cuyo, Av. Ezequiel Bustillo 9500, R8402AGP San Carlos de Bariloche, Río Negro, Argentina

HIGHLIGHTS

- Pure-phase LSCF nanocrystallites (~45 nm) have been synthesized by combustion.
- Nanopowder consists of interconnected nanocrystallites with meso- and macroporosity.
- Its electrocatalytic behavior as nanostructured cathode was evaluated by EIS measurements.
- ASR values as low as 0.8 Ω cm^2 at 450 °C and 0.04 Ω cm^2 at 650 °C were obtained.
- The improvement is due to the electrode morphology optimization in the nanoscale.

GRAPHICAL ABSTRACT

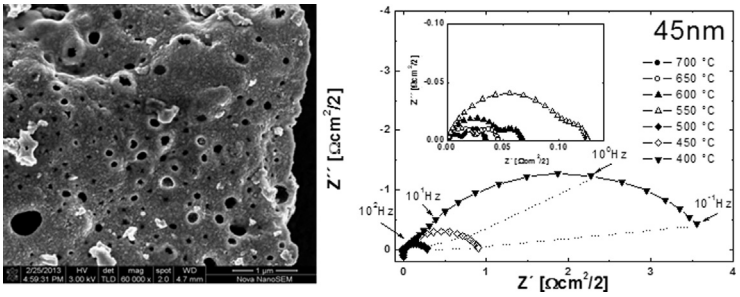

ARTICLE INFO

Article history:
Received 6 May 2014
Received in revised form
8 July 2014
Accepted 21 July 2014
Available online 30 July 2014

Keywords:
$La_{0.4}Sr_{0.6}Co_{0.8}Fe_{0.2}O_{3-\delta}$
Combustion synthesis
Nanocrystallites
Electrocatalysts
Solid oxide fuel cell

ABSTRACT

Pure-phase $La_{0.4}Sr_{0.6}Co_{0.8}Fe_{0.2}O_{3-\delta}$ (LSCF) nanocrystallites were successfully synthesized by the combustion method, by employing glycine as fuel and complexing agent, and ammonium nitrate as combustion trigger. The morphological and structural characterization of the LSCF nanopowders was performed by using X-ray diffraction, N_2 physisorption and electron microscopy. The LSCF nanopowder consists of interconnected nanocrystallites (~45 nm) forming a sponge-like structure with meso and macropores, being its specific surface area around 10 m^2 g^{-1}. Crystalline structural analyses show that the LSCF nanopowder presents cubic symmetry in the *Pm-3m* space group. By employing the spin coating technique and different thermal treatments, symmetrical cells with different electrode crystallite size (45 and 685 nm) were built, by using $La_{0.8}Sr_{0.2}Ga_{0.8}Mg_{0.2}O_{3-\delta}$ as electrolyte. Electrochemical impedance spectroscopy measurements were performed varying temperature and pO_2. The area specific resistance of the nanostructured sample (45 nm) decreases by two orders of magnitude with respect to the submicrostructured sample (685 nm), reaching values as low as 0.8 Ω cm^2 at 450 °C. This improvement is attributed to the cathode morphology optimization in the nanoscale, i.e., enlargement of the exposed surface area and shortening of the oxygen diffusion paths, which reduce the polarization resistance associated to the surface exchange and O-ion bulk diffusion process.

© 2014 Elsevier B.V. All rights reserved.

* Corresponding author. Centro Atómico Bariloche, Comisión Nacional de Energía Atómica, Argentina. Tel./fax: +54 294 4445288.
E-mail addresses: cchanquia@cab.cnea.gov.ar, cchanquia@gmail.com (C.M. Chanquía).

http://dx.doi.org/10.1016/j.jpowsour.2014.07.132
0378-7753/© 2014 Elsevier B.V. All rights reserved.

1. Introduction

Solid oxide fuel cells (SOFC) are electrochemical devices that operate at high temperatures, (800–1000 °C) directly converting chemical energy from air and fuels into electrical power. These devices achieve high efficiency and minimize the SO_x, NO_x and CO_2 emissions, with respect to conventional methods of power generation [1,2]. The SOFC cells are mainly composed of three components: a porous cathode, a porous anode and a dense solid electrolyte. The cathode is typically an oxide that catalyzes the oxygen reduction reaction, while the anode is an oxide or cermet that catalyzes the oxidation of fuel, either hydrogen or reformed hydrocarbons. The insulating dense electrolyte separates the air and fuel compartments and it allows the oxygen ions migration from cathode to anode, while the electrons migrate in the opposite direction through the external circuit, thereby generating electricity and water as by-product, when hydrogen is employed as fuel. Ideally, high fluxes of electroactive species on the electrode surface, due to the high hetero-catalytic activity of the cathode, decrease the voltage losses and maximize the electrical power generated for the fuel cell.

The main advantages of these silent and environmentally friendly SOFC devices are their high efficiency (>60%), modular design, the possibility to use not only H_2 but also different hydrocarbons types and the inclusion of internal reforming [1,2]. However, the main disadvantage is their high operating temperature, which promotes thermal activated processes such as solid state diffusion with the consequent grain growth of the electrodes and degradation or reactivity between the cell components. So, one challenge for materials scientists is to reduce the operation temperature of SOFC to 500 °C, which would have several benefits, such as operation costs reduction, minor start-up time, cell durability improvement, and at the same time it opens the possibility for the application of nanostructured materials with their associated electrocatalytic advantages.

It is noteworthy that the operation temperature decrement of SOFCs reduces its overall electrochemical performance. This is mainly due to the polarization loss from the air electrode (cathode), generated by the higher activation energy and in consequence lower reaction kinetics for oxygen reduction as compared with those of fuel oxidation in the anode [3,4]. When traditional electronic conductors are employed as cathode, such as $La_{1-x}Sr_xMnO_3$ (LSM) materials, the oxygen reduction reaction is limited to the region close to triple-phase boundaries (TPBs), i.e., where the oxygen, the cathode material and the electrolyte are in contact. In recent years, it has been given special attention to mixed ionic and electronic conductors (MIECs), in which the oxygen reduction reaction zone is enlarged beyond the TPB. The physico–chemical parameter which describes this enlarged region is known as the *electrode characteristic length* [5]. In consequence these materials maximize the electrocatalytic activity in comparison to pure electronic conductors.

$La_{1-x}Sr_xCo_{1-y}Fe_yO_{3-\delta}$ perovskite-type oxides have attracted substantial interest as promising cathode materials for intermediate temperature-SOFC, i.e., between 500 and 750 °C, due to their excellent properties, such as high mixed electronic and ionic conductivity, good chemical and thermal stabilities and high catalytic activity for the oxygen reduction reaction [2,6–9]. In compositions with high Sr and Co contents, the electronic conductivity is mainly associated with the multivalence of Co, while the ionic conductivity is linked to the transport of oxygen ions due to a vacancy diffusion mechanism [8,9]. In particular, the composition with $x = 0.6$ and $y = 0.2$ presents the advantage of no structural transformations being present between room temperature and 900 °C, in the oxygen partial pressure range between 10^{-5} and 1 atm [10]. According to the literature, the oxygen reduction reaction on these cathode materials is probably limited by the surface oxygen exchange process and by the oxygen ions bulk diffusion [11–13]. Usually, the activation energy of the oxygen surface process in MIEC materials is considerably higher than that of oxygen gaseous diffusion [14–16]. Therefore, a key to improve the IT-SOFC performance is to increase the surface area/volume ratio of the cathode by the bottom-up fabrication of nanostructured porous perovskite-type oxides.

In this context, the so-called combustion synthesis has been considered as an attractive way to synthesize a wide variety of ultrafine particles of metallic oxides including perovskites [17–20]. This simple method presents the advantage of using inexpensive precursors to produce nanosized powders, which are crystalline, homogeneous, softly agglomerated and highly reactive.

In the present study, the former aim is the optimization of the combustion synthesis conditions to obtain a pure-phase $La_{0.4}Sr_{0.6}Co_{0.8}Fe_{0.2}O_{3-\delta}$ (LSCF) nanopowder by employing glycine as complexing agent and fuel. The addition of ammonium nitrate in the combustion precursor gel, as an oxidizer agent and to trigger the combustion, is also evaluated. To be best of our knowledge, in literature there are not systematic studies on the influence of both glycine and ammonium nitrate contents in the initial synthesis gel in order to obtain pure-phase $La_{0.4}Sr_{0.6}Co_{0.8}Fe_{0.2}O_{3-\delta}$ nanocrystallites with low synthesis temperatures. A detailed morphological and structural characterization of the nanostructured LSCF materials is performed. Afterwards, the bottom-up construction of LSCF cathode with different crystallite size in symmetrical (LSCF/LSGM/LSCF) cells was done. Finally, the electrocatalytic behavior of these LSCF cathodes as a function of oxygen partial pressure (pO_2) and temperature is presented and discussed.

2. Experimental section

2.1. Synthesis of nanocrystallites

Nanostructured powders of $La_{0.4}Sr_{0.6}Co_{0.8}Fe_{0.2}O_{3-\delta}$ composition were synthesized by the combustion method by employing glycine (NH_2CH_2COOH) as fuel and complexing agent, and ammonium nitrate (NH_4NO_3) to trigger and to promote the combustion process. Glycine, one of the cheapest aminoacids, is known to act as a complexing agent for a number of metal ions, as it has a carboxylic acid group at one end and an amino group at the other end [17]. This zwitterionic characteristic of the glycine molecule enables the effective formation of complexes with metal ions of varying ionic sizes. These complexes help to maintain compositional homogeneity among the constituents by preventing their selective precipitation. Glycine also serves as a fuel in the combustion reaction, as it is oxidized by nitrate ions (oxygen from air does not play an important role during this combustion process). On the other hand, ammonium nitrate is often chosen as a combustion aid in combustion synthesis because of its low cost, highly exothermic decomposition and to generate gaseous products only, without altering the proportion of other elements that are produced [21].

In a typical procedure, stoichiometric amounts of La_2O_3 (Alfa Aesar, 99.99%), $SrCO_3$ (Alfa Aesar, 99%), metallic Co powder (Alfa Aesar, 99.8%) and metallic Fe pieces (Alfa Aesar, 99.99%) were dissolved in HNO_3 (Cicarelli, 65%) dilute solution. In order to obtain the nitrates mixture, the metal ions solution was kept at T ~80 °C during 24 h. Then, distilled water, different amounts of NH_2CH_2COOH (Aldrich, 98%) and NH_4NO_3 (Mallinckrodt, 99,99%) were added to the dried metal-nitrates mixture.

The obtained solutions with different glycine to oxidizers molar ratios were transferred to a preheated electric heating case and

kept at 180 °C. After ~2 h of heating, the spontaneous combustion of the precursor began and a large amount of gases was released.

Assuming complete combustion, the overall process may be presented by the following formal redox reaction for the formation of $La_{0.4}Sr_{0.6}Co_{0.8}Fe_{0.2}O_{3-\delta}$ perovskite:

$$2/5La(NO_3)_3 + 3/5Sr(NO_3)_2 + 4/5Co(NO_3)_2 + 1/5Fe(NO_3)_3 + nC_2H_5NO_2 + 9n/4O_2 \rightarrow La_{0.4}Sr_{0.6}Co_{0.8}Fe_{0.2}O_{3-\delta} + 2nCO_2 + 5n/2H_2O + (n/2 + 23/10)N_2 \quad (1)$$

CO_2, H_2O and N_2 are considered as the most stable products of the combustion synthesis with respect to other theoretical acceptable combinations, such as NO_x, N_2O_5 and CO [22]. According to concepts of propellant chemistry [22], it is possible to determine the so-called elemental stoichiometric coefficient, φ, as the ratio between the total valences of the fuel ($C_2H_5NO_2$) and the total valences of the oxidizers (nitrates):

$$\varphi = n[2(+4)_C + 5(+1)_H + 1(0)_N + 2(-2)_O]/\{w[1(+3)_{La} + 3((0)_N + 3(-2)_O)] + x[1(+2)_{Sr} + 2((0)_N + 3(-2)_O)] + y[1(+2)_{Co} + 2((0)_N + 3(-2)_O)] + z[1(+3)_{Fe} + 3((0)_N + 3(-2)_O)]\} \quad (2)$$

where n, w, x, y and z are moles of glycine, lanthanum nitrate, strontium nitrate, chromium nitrate and manganese nitrate, respectively. According to the Jain's method, the numbers in bracket in Equation (2) indicate the valence assumed by the elements in the most stable products of the combustion reaction: C and H elements are considered as reducing elements with the corresponding valences +4 and +1, oxygen is considered an oxidizing element with the valence −2, and nitrogen is considered with zero valence. Under stoichiometric conditions, the elemental stoichiometric coefficient is $\varphi = 1$; and in fuel-rich conditions $\varphi > 1$.

The $La_{0.4}Sr_{0.6}Co_{0.2}Fe_{0.8}O_{3-\delta}$ phase evolution was evaluated by subjecting the as-synthesized nanopowders to thermal treatments during 6 h in air-atmosphere in a furnace at 500, 700, 800 and 1000 °C (heating rate of 5 °C min^{-1}). The powder samples were labeled LSCM(ss), where "ss" indicates the synthesis stage: AS corresponds to "as-synthesized materials" and 500, 700, 800 and 1000 correspond to each thermal treatment, in Celsius degrees for 6 h.

2.2. Cell construction

To test the electrode behavior, a symmetrical 2-electrode configuration, by using LSGM ($La_{0.8}Sr_{0.2}Ga_{0.8}Mg_{0.2}O_{3-\delta}$, Next Tech Materials Ltd.) as electrolyte, was built. Dense LSGM disks of ~0.5 mm thickness and ~10 mm diameter were obtained by uniaxially pressing powder at 7.35 MPa. The disks afterwards were sintered at 1500 °C for 6 h. In order to improve the adhesion in the electrode/electrolyte interface, as well as also to reduce the contact resistance associated to the oxygen transfer process between both materials, a porous layer of LSGM commercial powder was deposited by the spin coating technique onto both faces of sintered LSGM disks and then fired at 1350 °C during 1 h [23]. Inks for electrode deposition were prepared by using 200 mg of nano or fine-crystallites (LSCF(800) or LSCF(1000), respectively), 26 mg of PVB (Polyvinyl butyral, Aldrich) as binder, 20 mg of PVP (Polyvinylpirrolidone, Alfa Aesar) as dispersant and 120 mg of α-terpineol (95%, Alfa Aesar) as densifier, in an isopropyl alcohol medium. Three LSCF-ink layers were deposited onto both surfaces of the LSGM electrolyte by the spin coating technique at ambient conditions, being each layer dried at 165 °C. Finally, these symmetrical cells were thermally treated under static air in a furnace at 800 and 1000 °C (heating rate 7 °C min^{-1}) during 6 and 2 h, respectively. The final cells were labeled Cell-*x*, where "*x*" is the average crystallite size of the electrode material.

2.3. Characterization techniques

The nanostructured LSCF powders were characterized by X-ray diffraction (XRD), nitrogen adsorption/desorption, scanning electron microscopy (SEM), transmission electron microscopy (TEM) and electrochemical impedance spectroscopy (EIS).

XRD patterns were collected in air, at room temperature, with a PANanalytical Empyrean diffractometer by using CuK(α_1 + α_2) lines, a graphite monochromator and a 3D PIXEL detector. Diffraction data were recorded in the range of 2Θ between 10 and 100° at an interval of 0.026° and scan step time of 1 s. The lattice parameters and the average crystallite size for each sample were determined from powder X-ray diffractograms by employing the Rietveld method and the FULLPROF program [24–26]. The XRD patterns were refined on the basis of a cubic crystalline system in the *Pm-3m* space group (N° 221), in agreement with the ICSD Collection Code N° 158793 [27]. The initial structural parameters for Rietveld refinement were taken from the mentioned reference. The refined parameters were the scale factor, background, shift lattice constants, profile half width parameters (U, V, W, X and Y), isotropic thermal factors, occupancy and atomic functional positions. The background was adjusted by using a linear interpolation through several points manually chosen. The diffraction peak profiles were fitted by the Thompson–Cox–Hastings pseudo-Voigt (pV-TCH) function and the asymmetry function described by Finger et al. [28].

Specific surface areas and pore size distributions were determined from N_2 adsorption/desorption isotherms, obtained at 77 K by using a Micromeritics ASAP 2020 (Accelerated Surface Area and Porosimetry System). The surface area was determined by the Brunauer, Emmett, and Teller (BET) method. The pore size distribution, obtained for the adsorption branch, was calculated by the Barrett, Joyner, and Halenda (BJH) method, based on the Kelvin equation.

The morphology of LSCF perovskites was observed by scanning electron microscopy (SEM) by using a SEM-FEG Nova NANO-SEM 230 equipment, operating at 5 kV and an electron landing energy of 1 keV. These conditions were used in order to observe insulator materials without any conducting coating.

Microstructure and morphology at high magnifications were studied by using Transmission Electron Microscopy (TEM) and High Resolution TEM (HR-TEM). Powder samples were dispersed in isopropanol and ultrasonicated for 15 min. Afterwards two drops were deposited over ultrathin carbon support films TEM grids and let dry in air. The images were obtained by using a Philips CM 200 UT microscope equipped with an ultra-twin objective lens. The electron source used was a LaB6 filament operated at 200 keV. The nominal resolution was 2 Å for the HR-TEM mode. The microscope was equipped with a CCD camera for image digital acquisition. Statistics on the crystallites was performed with the programs Image J 1.43U and Origin 8.0. Crystallite size corresponds to the mathematical average ± standard deviation (±SD) of the largest crystallite dimension.

Area specific resistance (ASR) electrode values were determined from electrochemical impedance spectroscopy (EIS) under symmetric atmosphere of synthetic air ($0.2O_2$–0.8Ar vol. %). It is noteworthy that the ASR values obtained from symmetrical measurements under the same gas composition (without chemical potential gradient) can be different to those obtained from fuel cell

tests. This is due to the fact that SOFC operates under an oxygen chemical potential gradient with oxidant and reducing gases in the cathode and anode respectively, and the current across the cell affects the polarization of both electrodes. Nevertheless, the symmetrical cell electrode measurement is a useful and easy method to compare different materials. The electrochemical cells prepared in symmetrical (LSCF/LSGM/LSCF) configuration were placed and slightly pressed on the porous electrodes between platinum grids, which were used as current collectors. The EIS spectra were collected along a frequency range 10^6 to 0.01 Hz with signal amplitude of 10 mV at 0 bias voltage by using a frequency response analyzer (FRA) coupled to an AUTOLAB. In a first study, EIS spectra were collected at 600 °C as a function of the oxygen partial pressure (pO_2). An electrochemical gas blending system based on a zirconia pump and oxygen sensor coupled to the symmetrical cell test system providing a controlled Ar–O_2 atmosphere with pO_2 values ranging from 7.10^{-4} to 1 atm. In a second study, the temperature was varied between 400 and 700 °C, whereas the atmosphere were kept dry by using a flow rate synthetic air ($0.2O_2$–0.8Ar vol. %) about 100 mL min^{-1}. The resulting spectra as a function of temperature and pO_2 were fitted with electrical equivalent circuit by using MatLab codes [29].

3. Results and discussion

3.1. Optimization of combustion conditions and structural characterization of the LSCF electrocatalyst

Fig. 1(A) presents XRD patterns of LSCF nanopowders synthesized by varying the elemental stoichiometric coefficient φ (the glycine content), with the addition of 1 g of ammonium nitrate (per gram of final perovskite catalyst) in the initial synthesis gels and subsequently calcined to 800 °C during 6 h. In the samples prepared with the higher content of glycine ($\varphi = 6.0$) as well as with the lower content ($\varphi = 2$), the LSCF phase is present, but with the segregation of a small amount of the $SrCoO_{2.5}$ as secondary phase (PDF N°: 00-048-0875 and 00-040-1018). The optimum synthesis condition by employing 1 g of NH_4NO_3 in the initial synthesis gel corresponds to $\varphi = 4$, for which the pure-phase LSCF nanocrystallites were obtained. It is noteworthy that a significant decrease in the size of the nanocrystallites (suggested by the broadening of the diffraction peaks) is evidenced for the sample synthesized with the higher glycine content ($\varphi = 6$). This behavior is probably due to the oversaturation of fuel in the gel, which generates a smooth and incomplete combustion process. On the other hand, Fig. 1(B) shows XRD patterns of the materials synthesized by varying the ammonium nitrate content in the initial synthesis gel while keeping constant the elemental stoichiometric coefficient φ equal to 4. For the lower ammonium nitrate contents in the initial synthesis gel (0 and 1 g per gram of final catalyst), it was generated a smooth combustion with a large release of ocher smoke. When the content of NH_4NO_3 was increased to 3 g (per gram of final catalyst), the combustion was faster with the appearance of sparks, probably due to the presence of a higher amount of oxidant in the middle of synthesis (NO_3^-). To obtain 1 g of LSCF catalyst, the optimum ammonium nitrate content in the initial synthesis gel for $\varphi = 4$ was 1 g. Both in absence of NH_4NO_3 as well as by employing a higher content (3 g per gram of final catalyst) of NH_4NO_3 in the gel, it reappears the $SrCoO_{2.5}$ secondary phase. These behaviors are probably due to several factors: i) a high content of glycine (above the stoichiometric amount) is necessary for correct organization of the metal ions in the organometallic complex generated in previous seconds to the combustion process, ii) the diffusion processes occurring during combustion of the organometallic complex would be influenced by the combustion temperature, which in turn strongly depends on the fuel/oxidant ratio (NH_2CH_2COOH/NO_3^-), iii) an excess of oxidant (NO_3^-) in the gel synthesis will generate undesirable oxides in the combustion ashes. It can be concluded from this first analysis, that to obtain pure-phase $La_{0.4}Sr_{0.6}Co_{0.2}Fe_{0.8}O_{3-\delta}$ perovskites the optimum condition of synthesis is to employ an elemental stoichiometric coefficient $\varphi = 4$ with the addition of 1 g of NH_4NO_3 (per gram of final catalyst) as combustion-aid in the initial synthesis gel. These conditions cause a smooth combustion without flame which generates a precursor ash. Finally the pure-phase LSCF perovskite is obtained when the precursor ash is subsequently calcined at 800 °C during 6 h.

Fig. 2 shows XRD patterns of the as-synthesized LSCF(AS) ash prepared with $\varphi = 4$ and 1 g of NH_4NO_3 (per gram of final perovskite catalyst) in the initial synthesis gel, and its respective thermal treatments at 500, 700, 800 and 1000 °C. As it can be observed, the precursor LSCF (AS) ash evidences an organic amorphous phase, but when this material was calcined to 500 °C it begins to appear the perovskite structure with several impurities. Later, when the treatment temperature was increased at 700 °C, the perovskite LSCF (700) phase crystallized almost completely, giving only a small amount of $SrCoO_{2.5}$ impurity-phase. At 800 °C, the pure-phase LSCF (800) nanocrystallites were obtained. Additionally, when the LSCF (AS) ash was subjected to subsequent

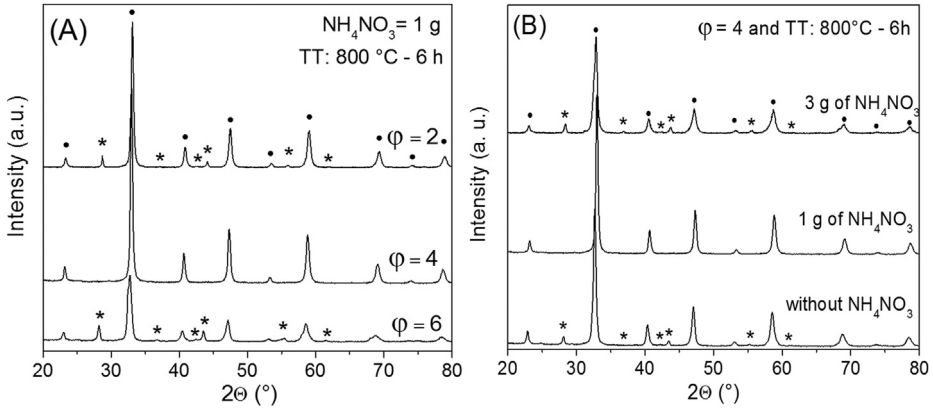

Fig. 1. XRD patterns of LSCF nanopowders calcined at 800 °C for 6 h synthesized by varying: (A) the elemental stoichiometric coefficient ($\varphi = 2$, 4 and 6) with the addition of 1 g of ammonium nitrate as combustion aid in the initial synthesis gel; (B) the ammonium nitrate content in the initial synthesis gel by keeping constant the elemental stoichiometric coefficient $\varphi = 4$. Phases present: ● $La_{0.4}Sr_{0.6}Co_{0.8}Fe_{0.2}O_{3-\delta}$; * $SrCoO_{2.5}$ (PDF N°: 00-048-0875, 00-040-1018).

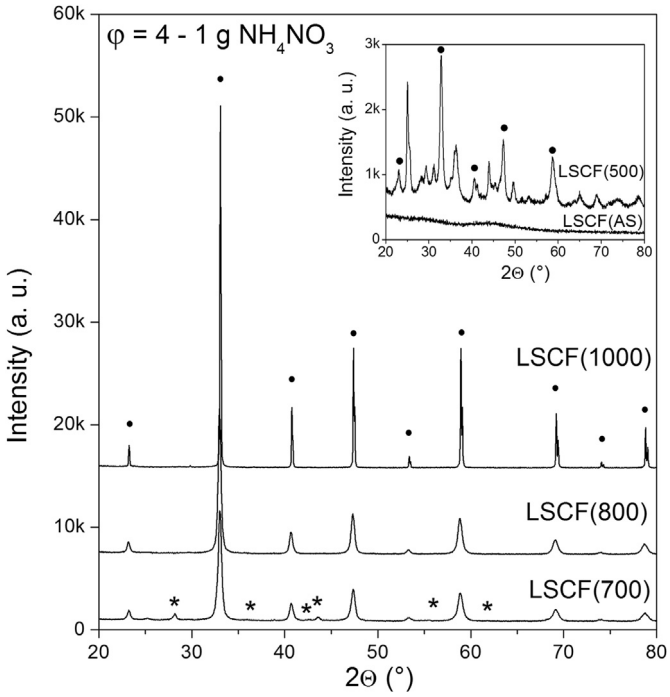

Fig. 2. XRD patterns of as-synthesized LSCF nanopowder synthesized from a $\varphi = 4$ and 1 g of ammonium nitrate in the initial synthesis gel and its respective thermal treatments during 6 h at 500, 700, 800 and 1000 °C. Phases present: ● $La_{0.4}Sr_{0.6}Co_{0.8}Fe_{0.2}O_{3-\delta}$, * $SrCoO_{2.5}$ (PDF N°: 00-048-0875, 00-040-1018).

thermal treatment at 1000 °C, the purity of the LSCF phase was preserved. However, in accordance to the narrowing of the diffraction peaks of the LSCF (1000) pattern, these crystallites displayed a considerable growth.

In order to determine the lattice parameters and the average crystallite size of LSCF nanopowders, the XRD patterns were analyzed with the FULLPROF program by employing Rietveld refinement technique. This method employs the intensity profile obtained from step-scanning measurements of the ceramic to refine the structure model of a material [21]. Some results of the Rietveld refinements of LSCF powders are presented in Table 1. In addition, a representative Rietveld refinement of LSCF(800) sample is shown in Fig. 3. The fitting parameter values (R_p, R_{wp}, R_{Bragg}, and χ^2) shown in Table 1, indicate a good agreement between the refined and observed XRD patterns for the LSCM phase, which confirms that the $La_{0.4}Sr_{0.6}Co_{0.8}Fe_{0.2}O_{3-\delta}$ nanocrystallites belongs to the cubic crystalline symmetry in *Pm-3m* space group (N° 221).

Table 1
Structural and morphological parameters of the LSCF nanopowders, prepared from $\varphi = 4$ and 1 g of NH_4NO_3 in the initial synthesis gel, thermally treated in static air at 500, 700, 800 and 1000 °C.

Muestra	S_{BET} ($m^2\ g^{-1}$)[a]	V_{BJH} ($cm^3\ g^{-1}$)[b]	D_p (nm)[c]	$a = b = c$ (Å)[d]	V (Å^3)[e]	d ($g\ cm^{-3}$)[f]
LSCF(500)	27.7	0.227	–	–	–	–
LSCF(700)	17.1	0.167	32.7	3.84	56.83	6.21
LSCF(800)	7.9	0.105	45.3	3.84	56.72	6.23
LSCF(1000)	0.2	0.0008	684.8*	3.84	56.75	6.19

[a] BET specific surface area.
[b] BJH adsorption cumulative volume of pores. Parameters obtained from Rietveld refinement.
[c] Average crystallite size.
[d] Direct cell parameters.
[e] Unit cell volume.
[f] Density (volumic mass). Fitting confidence: $\chi^2 < 2.3$, $R_{Bragg} < 1.7$, $R_p < 7$ and $R_{wp} < 8.5$.* Obtained from SEM images.

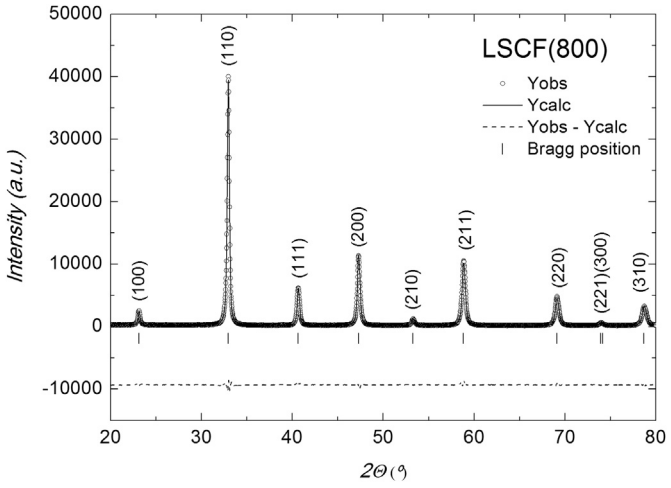

Fig. 3. Rietveld-refined XRD profile of LSCF (800) nanopowder synthesized from $\varphi = 4$ and 1 g of ammonium nitrate in the initial synthesis gel. The ○ signs represent experimental points and the solid line represents Rietveld-refined data. The dotted lines show the difference between experimental and refined data.

On the other hand, the apparent crystallite sizes (D_p) of LSCF nanopowders, also calculated from Rietveld refinement, are shown in Table 1. As it can be observed, the average crystallite size of the LSCF nanopowders drastically increased from 30 to 700 nm when the calcination temperature increased from 700 to 1000 °C, respectively. This fact demonstrates the high sinterability that this composition presents above 800 °C.

Fig. 4 shows the N_2 adsorption/desorption isotherms of LSCF electrocatalysts, prepared with $\varphi = 4$ and 1 g of NH_4NO_3 (per gram of final perovskite catalyst) in the initial synthesis gel, thermally

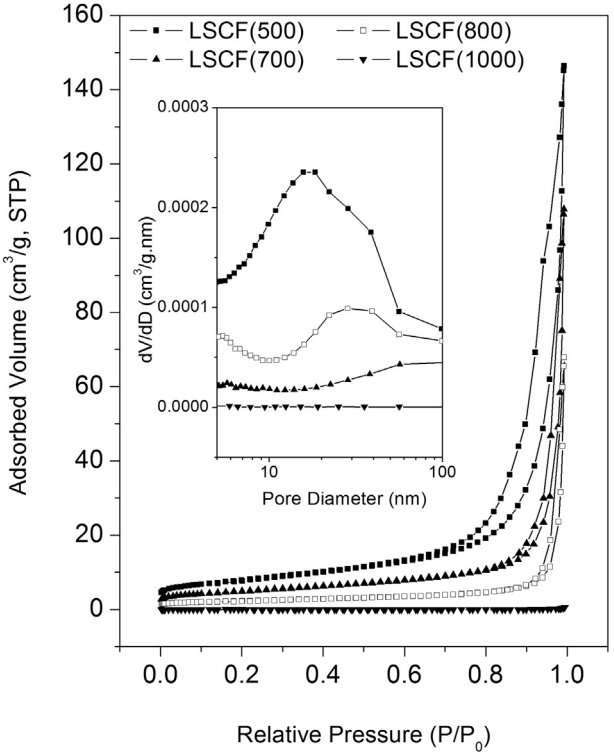

Fig. 4. Nitrogen physisorption isotherms and BJH pore size distribution (inset) of LSCF nanopowders synthesized from $\varphi = 4$ and 1 g of ammonium nitrate in the initial synthesis gel and calcined at different temperatures: 500, 700, 800 and 1000 °C.

treated in static air at 500, 700, 800 and 1000 °C, as well as their corresponding BJH pore size distribution (inset). All of the samples exhibit type II isotherms in IUPAC classification, typical of macroporous structures with stronger interactions with the adsorbate [30]. In addition, the isotherms of the LSCF (500/700/800) samples exhibit a combination of H1/H3-type hysteresis loops in IUPAC classification. The type H1 loop is often associated with porous materials, known to consist of agglomerates (i.e., an assemblage of particles rigidly joined together) or compacts of approximately uniform spheres in a fairly regular array. They present a narrow distribution of pore size. The type H3 loop presents aggregates of plate-like particles giving rise to slit-shaped pores, which does not exhibit any limiting adsorption at high p/p_0 [30]. These behaviors would indicate the existence of a macropore network within the powder assembly with the additional presence of inter-crystallite mesoporosity. In fact, the inset of Fig. 4 shows a wide BJH-size distribution in the mesoporous region (2–50 nm) for these nanopowders, which evidences a shift to the right for the samples calcined at higher temperatures, i.e., towards the macroporous region (>50 nm), reaching practically the nullity in the LSCF sample (1000). It is noteworthy that the hysteresis loop area decreases when the calcination temperature increases, which evidences the decrease of the mesoporosity. The BET specific surface areas of LSCF samples are shown in Table 1. As it can be observed, the increase of the calcination temperature decreases appreciably the specific surface area from ~20 to ~0.2 $m^2\ g^{-1}$, for LSCF(700) and LSCF(1000) samples, respectively, which is in agreement with the marked increment of the average crystallite size from ~30 to ~700 nm obtained from Rietveld refinement. For temperatures above 800 °C, the grain growth process (i.e., atom diffusion and grain-boundary migration) is strongly activated. A huge coalescence produces agglomerated crystallites and, consequently, a high grain growth appear in these submicrostructured LSCF(1000) powder.

The morphology evolution of the LSCF electrocatalyst as a function of the calcination temperature was examined by scanning electron microscopy. SEM images corresponding to the LSCF(AS) sample calcined at 500, 700, 800 and 1000 °C, during 6 h, are presented in Fig. 5. The LSCF material calcined at 500 °C displays foam-like morphology. At 700 °C it consists in cuasi-spherical nanocrystallites of size around 30 nm slightly agglomerated with a lot of mesopores among them, in agreement with the N_2 physisorption measurements. At 800 °C, it can be observed a meso- and macroporous material consistent in an assembly of nanocrystallites strongly interconnected. As it can be observed in Fig. 5, the pure-phase $La_{0.4}Sr_{0.6}Co_{0.8}Fe_{0.2}O_{3-\delta}$ perovskite obtained at this calcination temperature shows a particle size distribution around 40 nm, in agreement with the Rietveld results, presenting high interconnectivity between nanocrystallites and open porosity, which help to improve the electrocatalytic behavior as cathode in the SOFC cells. Finally, it is noteworthy the high sintering ability of this composition when the calcination temperature is around 1000 °C. At this temperature, the coalescence process of the grains is strongly activated generating crystallites in the micro-scale practically without interparticle porosity, which is demonstrated by the important decrease of the specific surface area of the LSCF (1000) sample.

Fig. 6 presents bright field (BF) TEM images of the LSCF (500/700/800) nanopowders. In the images (a,b), corresponding to the LSCF (500) sample, both amorphous and crystalline regions were observed, in agreement with XRD measurements. The images (c,e) of LSCF (700) and LSCF (800), respectively, show an increase of the crystallite size with a strong interconnectivity among nanocrystallites. These images also present low contrast randomly regions, which are attributed to meso-scale cavities. The high purity, strong interconnectivity among crystallites and open porosity obtained for LSCF (800) will enhance its electrocatalytic performance. The crystallinity of these LSCF materials was analyzed by HR-TEM measurements. As it can be observed in the images (d,f), LSCF(700) and LSCF(800) samples are constituted by single nanocrystallites, i.e., within each nanocrystallite, lattice fringes (individual atomic planes) show a single crystal orientation.

Fig. 7 shows SEM images of the electrode/electrolyte interfaces and electrode morphologies of Cell-45 (a,b,c) and Cell-685 (d,e,f) before the electrocatalytic testing. The electrodes show porous microstructures with adequate adherence to the LSGM electrolyte disk. Although an equal mass of crystallites (1 g) was employed in all of LSCF-inks, the electrode thicknesses obtained in the final cells varied markedly. The electrode thickness of the Cell-685 (image d), constructed by employing fine-crystallites, was around 10 μm, while for Cell-45 (image a), constructed from nanocrystallites, was above to 40 μm. This behavior indicates that the final porosity degree obtained in the electrodes constructed from

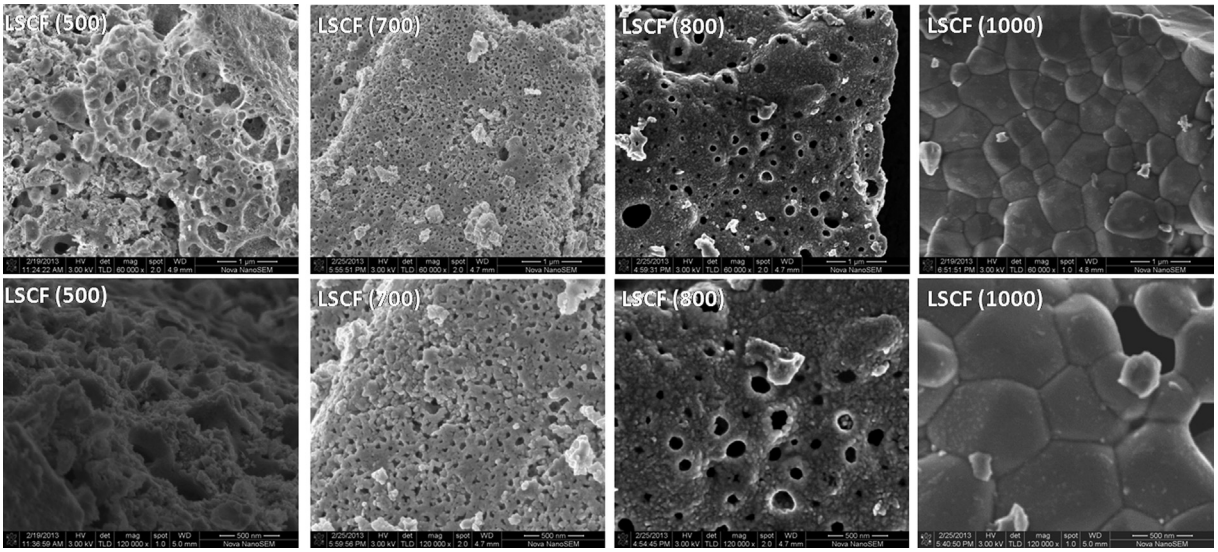

Fig. 5. SEM images of LSCF nanopowders synthesized from $\varphi = 4$ and 1 g of ammonium nitrate in the initial synthesis gel and calcined at 500, 700, 800 and 1000 °C, they are shown at different magnitudes (top: 60,000×; bottom: 120,000×).

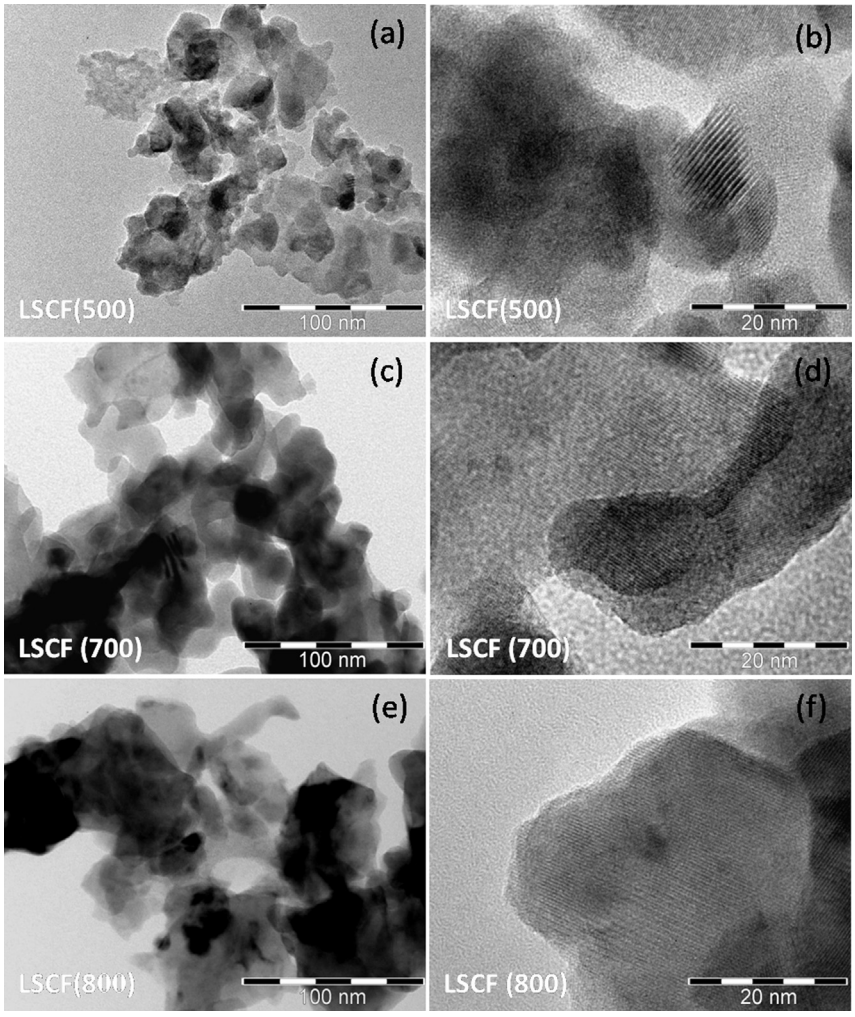

Fig. 6. TEM (left) and HR-TEM (right) images of LSCF nanopowders synthesized from $\varphi = 4$ and 1 g of ammonium nitrate in the initial synthesis gel and calcined at 500, 700 and 800 °C.

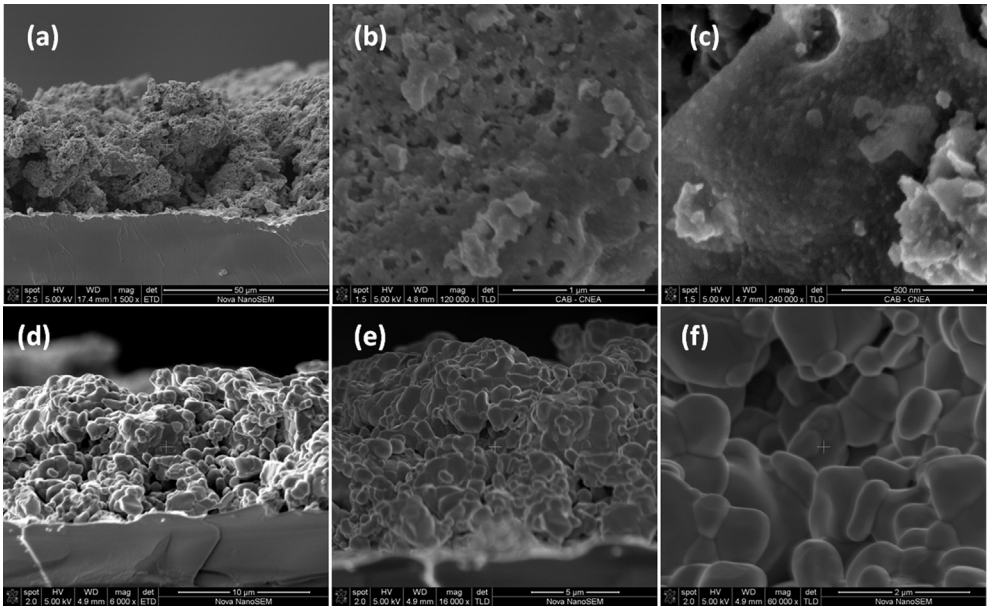

Fig. 7. SEM images of the electrode/electrolyte interfaces and electrode morphologies of the Cell-45 (a,b,c) and Cell-685 (d,e,f).

nanocrystallites is bigger, which probably would enhance the diffusion of the reactive gases into the electrodes. As it can be observed in images (b,c) and (e,f), the morphology characteristics (i.e., crystallite size, interconnectivity between crystallites, porosity, etc.) of both precursors LSCF powders (nano and ultrafine) were remained after stuck of the material to the electrolyte-disks. In addition, it is worth to mention that no significant changes were observed in the electrode morphologies, after the cells were subjected to the electrocatalytic tests under oxidizing atmospheres.

3.2. Electrocatalytic behavior

The oxygen reduction reaction on cobalt rich phase-perovskite $La_{1-x}Sr_xCo_{1-y}Fe_yO_{3-\delta}$ cathodes has been widely studied by using electrochemical impedance spectroscopy (EIS) [31–38]. This technique allows separating the global electrode reaction in different contributions (impedance arcs), due to the different relaxation times (inversely proportional to maximum frequency) of each process. In the case of the oxygen reduction reaction for SOFC cathodes, the low frequency (LF) arcs are often attributed to the oxygen gas diffusion or either surface processes such as oxygen adsorption/desorption or surface diffusion of intermediate oxygen species [39–45]. On the other hand, the high frequency (HF) arcs are usually associated with charge-transfer processes, oxygen ion diffusion in the bulk cathode or the incorporation of oxygen ions from the three-phase boundary [39–45]. It is possible to separate the different contributions of the EIS spectra by varying the temperature and oxygen partial pressure (pO_2). These measures are commonly used in order to identify the nature of the electrode process and to correctly assign the equivalent electronic circuit employed to fit the EIS spectra.

The electrocatalytic behavior of the LSCF cathodes with different morphologies was evaluated by EIS in symmetric (LSCF/LSGM/LSCF) cells under zero dc polarization. The effect of pO_2 was evaluated at 600 °C in the range between 0.86 and 6.9×10^{-4} atm, and the effect of temperature was explored between 400 and 700 °C under synthetic air atmosphere ($0.2O_2$–$0.8Ar$ vol. %). All spectra were collected after reaching the equilibrium. The original axis values (Ω) of the Nyquist plots obtained in the recorded data were multiplied by the electrode geometrical area (cm^2) and then halved due to the symmetric configuration of the cells. For the sake of comparison, the high frequency intersection of the spectra with the real axis in the Nyquist plane, which represents the sum of the electrolyte resistance and electrical circuits, has been subtracted, and therefore all the spectra as a function of both, temperature and pO_2, only represent the area specific resistance (ASR) of the electrode.

Fig. 8 shows the normalized EIS spectra at 600 °C for the LSCF electrodes, with average crystallite sizes around 45 nm (Cell-45) and 685 nm (Cell-685), varying the pO_2 between 0.86 and 6.9×10^{-4} atm. Both impedance values increase as pO_2 decreases, but whereas the EIS spectra corresponding to Cell-45 are clearly split in two arcs, only one impedance arc can be distinguished for Cell-685. Considering this, the EIS spectra corresponding to Cell-45 were fitted with an equivalent circuit model, assuming a Gerischer (G) dependence for the high frequency (HF) contribution, in series with a parallel resistor/capacitor (RC) element for the low frequency (LF) arc. On the other hand, the spectra for Cell-685 can be properly fitted only by using a Gerischer-type equivalent circuit. It is worth to mention that the inductance of wires (L) and the electrolyte resistance (R_{el}) were also included in the adjustment. The plot of log R vs. log pO_2 is shown in Fig. 9. The polarization resistance depends on the oxygen partial pressure as $R \propto pO_2^{-n}$, where the n values suggest the limiting step of the mechanism of oxygen reduction reaction dominating the impedance arc. Thus, $n = 1$ is associated to limiting steps involving molecular oxygen as the oxygen gas diffusion or non-dissociative adsorption, n around 0.5 is referred to the O-atomic as the dissociative adsorption or O-surface diffusion limiting steps and an independently R with pO_2 suggests that O ions are involved such as in the O-ion bulk diffusion or ion transfer from electrode to electrolyte [46–50]. The Gerischer impedance element describes the electrochemical response for an electrode reaction where the oxygen ions diffusion inside the MIEC is limited by the oxygen surface exchange processes [51,52]. Then, both Gerischer resistance (R_G) and relaxation time (τ_G) depend on the microstructural features including exposed surface area, porosity and tortuosity, and material properties such as oxygen ion diffusion and surface exchange coefficients. The global pO_2-dependence of the Gerischer resistance is the weighted combination of both, the oxygen ion diffusion and surface exchange processes. The RC element used to fit the LF arc of Cell-45 varies as pO_2^{-1}, indicating the participation of O-molecular species in the O_2 gas diffusion.

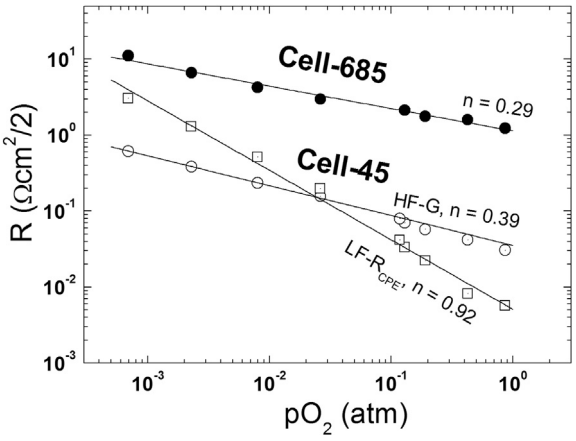

Fig. 9. Log plot of the electrode polarization resistance contributions of the Cell-45 and Cell-685 as a function of the pO_2.

The normalized EIS spectra collected in air at temperatures ranging between 400 and 700 °C for Cell-45 and Cell-685 are

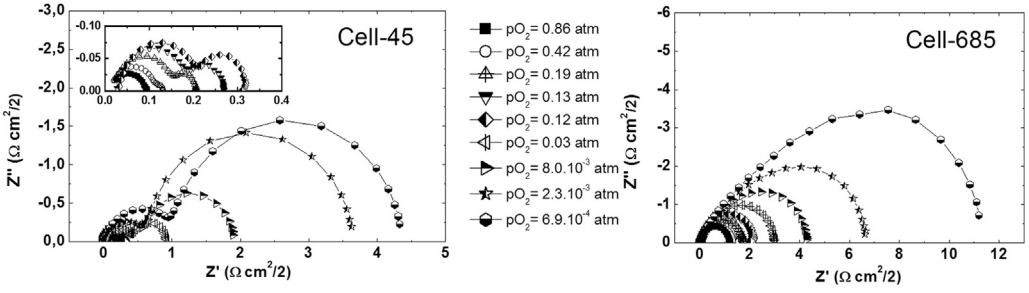

Fig. 8. Electrochemical impedance spectra of the Cell-45 and Cell-685 collected at 600 °C varying the pO_2 between 0.86 and 6.9×10^{-4} atm.

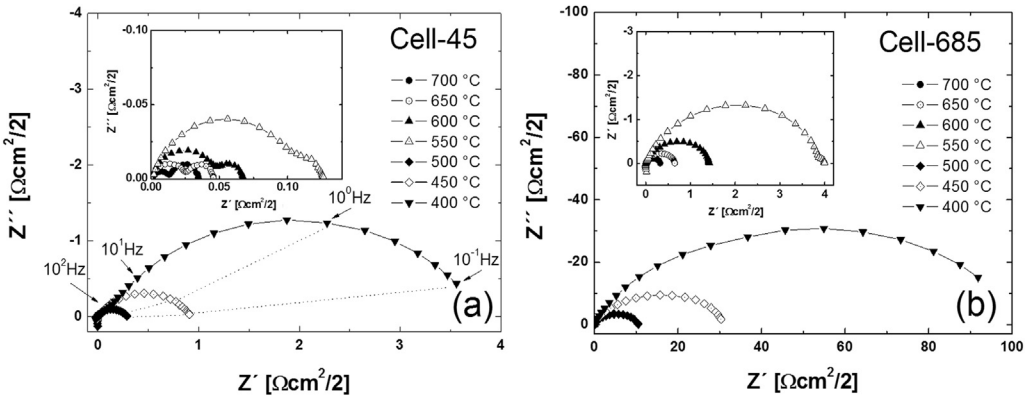

Fig. 10. Electrochemical impedance spectra of LSCF cathodes with average crystallite size around 45 (a) and 685 nm (b) deposited symmetrically on LSGM electrolyte disks. The EIS data was collected between 400 and 700 °C under symmetric ($0.2O_2$–0.8Ar vol. %) air synthetic atmosphere.

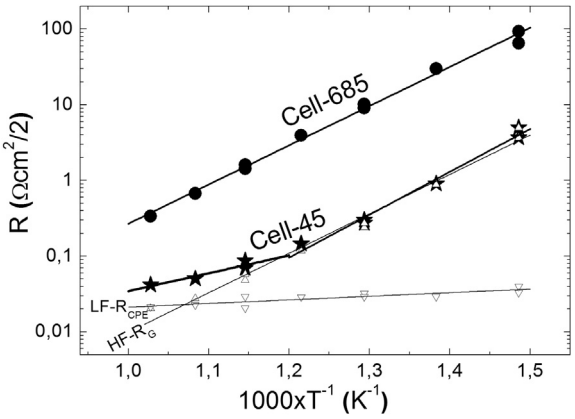

Fig. 11. Arrhenius plot of the Area Specific Resistances (ASR) of the Cell-45 (★) and Cell-685 (●). Additionally, the HF (△) and LF (▽) contributions of the Cell-45 are also discriminated.

presented in Fig. 10. As it can be observed from Fig. 10(a) and (b), at each temperature, Cell-45 shows electrode polarization resistances practically two orders of magnitude lower those of Cell-685. In addition, the presence of two well distinguished arcs in the impedance spectra for Cell-45 at temperatures above 550 °C, suggests that at least two different electrode processes limit the oxygen reduction reaction. Then, the same electrical equivalent circuit used to fit the EIS spectra at 600 °C and different pO_2 can be also used to fit the spectra as a function of temperature in synthetic air.

Fig. 11 shows the Arrhenius plot of the overall area specific resistance (ASR) for Cell-685 and Cell-45 as well as the high and low frequency contributions to the global impedance of Cell-45, i.e., the Gerischer (HF-R_G) and R//CPE (LF-R_{CPE}), respectively. The slope change for Cell-45 at 550 °C indicates that below the temperature the LF contribution to the polarization resistance can be neglected, while above this temperature the LF contribution becomes significant.

Table 2 summarizes some general data obtained from fitting the impedance spectra with the electrical equivalent circuits as a function of temperature and pO_2. As it can be observed from Table 2 and Figs. 9 and 11, the overall R_G resistance of the submicrostructured Cell-685 and the HF-R_G contribution of the nanostructured Cell-45 exhibit the same activation energy (1.03 eV), and similar pO_2 dependence. These behaviors suggest that the same mechanism is operating for both impedance contributions. The polarization resistance of Gerischer-type impedance for Cell-45 decreases almost two orders of magnitude in comparison to R_G values of Cell-685. In the same way, both the relaxation time τ_G and the associated capacitance decrease as the electrode crystallite size decreases.

In addition, the LF contribution of Cell-45 exhibits low polarization resistances, high capacitances (1–10 F cm^{-2}), low activation energy (0.4 eV) and a pO_2 dependence close to the unity ($n = 0.9$), which are typical values of a controlled O_2 gaseous diffusion process. As it can be observed in Figs. 5 and 7, the electrode of Cell-45 presents two different pore sizes: macropores (>50 nm) and mesopores (between 2 and 50 nm). The formers are created during the combustion process as well as during the calcination of the organic

Table 2
Electrochemical data of the Cell-45 and Cell-685 obtained from fitting the impedance (Z) spectra with the electrical equivalent circuits as a function of the temperature and pO_2.

Sample	ASR		Equivalent circuit		
	R (Ω cm^2) at 600 °C	E_a (eV)	$Z_{parameters}$ at 600 °C	E_a (eV)	n (RpO_2^{-n})
Cell-685	1.5(1)	1.03(3) 400–700 °C	L Rel GHF		
			$R_G = 1.5(1)$ Ω cm^2	1.03(3)	0.29
			$\tau_G = 0.15$ s		
			$C = 0.1$–0.4 F cm^{-2}		
Cell-45	0.08(1)	1.16(6) 400–550 °C 0.40(6) 600–700 °C	L Rel GHF RLF CPELF		
			$R_G = 0.053(7)$ Ω cm^2	1.03(3)	0.39
			$\tau_G = 10^{-3}$ s		
			$C = 0.01$–0.05 F cm^{-2}		
			$R_{CPE} = 0.025(6)$	0.09(2)	0.91
			$C = 1$–10 F cm^{-2}		

compounds contained in the electrode ink, while the mesopores are created only from gas released during the combustion process. On the other hand, the Cell-685 only presents macropores mainly formed during the burning of the electrode ink. Considering normal gas diffusion through macropores and Knudsen diffusion inside mesopores, it can be assumed that the LF impedance for the Cell-45 should be similar or higher than that of Cell-685. As the resistance values of the LF contribution of Cell-45 are negligible in comparison with the overall Cell-685 resistances, the LF-resistance contribution of Cell-685 can be disregarded.

Therefore, from the analysis of the effect of temperature and pO_2 on the electrocatalytic behavior of Cell-45 and Cell-685, it can be concluded that the improvement of polarization resistance is due to the nano-scale effect enlargement of the active surface of the electrode, increasing the number of contact points at the electrode/electrolyte interface, and shortening of the oxygen diffusion paths.

Finally, it is worth to mention, that the nanostructured cathode achieved for us in the Cell-45 showed ASR values as low as ~0.8 Ω cm^2 at 450 °C and ~0.04 Ω cm^2 at 650 °C, which confers to this material a potential application as electrode of intermediate temperature-SOFC cells. These ASR values arise from employing a simple synthesis method as the combustion and the spin-coating as deposition technique, and they are considerably minor than the most values reported in literature, e.g.: Guo et al. [53] reported polarization resistances ~0.28 Ω cm^2 at 800 °C, by employing the solid state reaction as synthesis method and $La_{0.9}Sr_{0.1}Ga_{0.8}Mg_{0.2}O_{3-\delta}$ as electrolyte; Marrero-López [42] et al. reported ASR values around 5 Ω cm^2 at 450 °C, by employing spray pyrolysis as synthesis method and $Ce_{0.8}Gd_{0.2}O_{1.9}$ as electrolyte; García et al. [39] reported 0.34 Ω cm^2 at 750 °C, by employing citrate-hydrothermal synthesis and $Ce_{0.9}Gd_{0.1}O_{1.95}$ as electrolyte; Baqué et al. [54], reported ASR values (e.g. 0.05 Ω cm^2 at 600 °C) of the same order of magnitude that the obtained for us, but by employing the HMTA synthesis method and $Ce_{0.9}Gd_{0.1}O_{2-\delta}$ as electrolyte.

4. Conclusions

In the present study, LSCF nanopowders have been successfully synthesized by the low-temperature auto-combustion method by using glycine as fuel and complexing agent, and ammonium nitrate as oxidizer and combustion trigger. By employing a stoichiometric elemental coefficient (φ) equal to 4 and 1 g of ammonium nitrate (per gram of final catalyst) in the combustion precursor gel, and with a subsequent thermal treatment at 800 °C during 6 h, pure-phase $La_{0.4}Sr_{0.6}Co_{0.8}Fe_{0.2}O_{3-\delta}$ nanocrystallites were obtained. These pure-phase LSCF nanopowders consist of strongly aggregated nanocrystallites forming a sponge-like structure. The average nanocrystallite size of the pure-phase LSCF was around 45 nm and its specific surface area was around 10 m^2 g^{-1}. Crystalline structural analyses showed that the LSCF nanopowders present the cubic symmetry in the *Pm-3m* space group. Electrodes with different crystallite size (45 and 685 nm) were built onto both sides of the $La_{0.8}Sr_{0.2}Ga_{0.8}Mg_{0.2}O_{3-\delta}$-disk electrolyte. The electrode polarization resistance decreases two orders of magnitude when the electrode crystallite size decreases from 685 nm to 45 nm, reaching values as low as 0.04 Ω cm^2 at 650 °C and 0.8 Ω cm^2 at 450 °C. The study of electrode reaction mechanism was performed by EIS as a function of temperature and pO_2. For the nanostructured electrodes, these studies allowed to assign the HF contribution to a Gerischer-like impedance, associated to a convoluted oxygen surface exchange and bulk diffusion process, whereas the LF contribution was attributed to Knudsen-type gas diffusion in the mesopores. This significant improvement on the polarization resistance is attributed to the cathode morphology optimization in the nanoscale, which enlarges the electrode exposed surface area, maximizes the contact points in the electrode/electrolyte interface and shortens the oxygen diffusion paths.

Acknowledgments

This work was supported by CONICET, CAB-CNEA and Ministerio de Ciencia, Tecnología e Innovación Productiva (MINCyT) of Argentina. C. M. Ch. thanks to Phys. María Da Fonseca and Eng. George Ebri for their valuable collaborations in the experimental activities, and to Dr. Fabiana Gennari for the N_2 physisorption measurements.

References

[1] N.Q. Minh, T. Takahashi, Science and Technology of Ceramic Fuel Cells, Elsevier, Amsterdam, 1995.
[2] S.C. Singhal, K. Kendall, High Temperature Solid Oxide Fuel Cells, Elsevier, Oxford, 2004.
[3] E. Ivers-Tiffee, A. Weber, D. Herbstritt, J. Eur. Ceram. Soc. 21 (2001) 1805–1811.
[4] J. Fleig, Ann. Rev. Mater. Res. 33 (2003) 361–382.
[5] S.B. Adler, Solid State Ionics 135 (2000) 603–612.
[6] A. Mai, V.A.C. Haanappel, S. Uhlenbruck, F. Tietz, D. Stover, Solid State Ionics 176 (2005) 1341–1350.
[7] A. Orera, P.R. Slater, Chem. Mater. 22 (2010) 675–690.
[8] L.-W. Tai, M.M. Nasrallah, H.U. Anderson, D.M. Sparlin, S.R. Sehlin, Solid State Ionics 76 (1995) 259–271.
[9] L.-W. Tai, M.M. Nasrallah, H.U. Anderson, D.M. Sparlin, S.R. Sehlin, Solid State Ionics 76 (1995) 273–283.
[10] F. Prado, N. Grunbaum, A. Caneiro, A. Manthiram, Solid State Ionics 167 (2004) 147–154.
[11] J.A. Lane, S.J. Benson, D. Waller, J.A. Kilner, Solid State Ionics 121 (1999) 201–208.
[12] J.W. Lee, Z. Liu, L. Yang, H. Abernathy, S.H. Choi, H.E. Kim, J. Power Sources 190 (2009) 307–310.
[13] M.E. Lynch, L. Yang, W.T. Qin, J.J. Choi, M.F. Liu, K. Blinn, Energy Environ. Sci. 4 (2011) 2249–2258.
[14] M. Katsuki, S. Wang, M. Dokiya, T. Hashimoto, Solid State Ionics 156 (2003) 453–461.
[15] Z. Shao, S. Haile, Nature 431 (2004) 170–173.
[16] A. Egger, E. Bucher, W. Sitte, J. Electrochem. Soc. 158 (2011) B573–B579.
[17] L.A. Chick, L.R. Pederson, G.D. Maupin, J.L. Bates, L.E. Thomas, G.J. Exarhos, Mater. Lett. 10 (1990) 6–12.
[18] A. Civera, M. Pavese, G. Saracco, V. Specchia, Catal. Today 83 (2003) 199–211.
[19] C.M. Chanquía, J.E. Vega-Castillo, A.L. Soldati, H. Troiani, A. Caneiro, J. Nanopart. Res. 14 (2012) 1104.
[20] C.M. Chanquía, A. Montenegro-Hernández, H.E. Troiani, A. Caneiro, J. Power Sources 245 (2014) 377–388.
[21] J.L. Bates, L.A. Chick, W.J. Weber, Solid State Ionics 52 (1992) 235–242.
[22] S.R. Jain, K.C. Adiga, V.R. Pai Verneker, Combust. Flame 40 (1981) 71–79.
[23] C.F. Setevich, L.V. Mogni, A. Caneiro, F.D. Prado, Int. J. Hydrogen Energy 37 (2012) 14895–14901.
[24] R.A. Young, The Rietveld Method, International Union of Crystallography & Oxford University Press, New York, 1996.
[25] H.M. Rietveld, J. Appl. Crystallogr. 2 (1969) 65–71.
[26] J. Rodríguez-Carvajal, Phys. B Cond. Matter 192 (1993) 55–69.
[27] T.V. Aksenova, M.V. Ananev, L.Y. Gavrilova, V.A. Cherepanov, Neorganic. Mater. 43 (2007) 347–351.
[28] L.W. Finger, D.E. Cox, A.P. Jephcoat, J. Appl. Crystallogr. 27 (1994) 892–900.
[29] http://www.mathworks.com/matlabcentral/fileexchange/19460-zfit.
[30] K.S.W. Sing, D.H. Everett, R.A.W. Haul, L. Moscou, R.A. Pierotti, J. Rouquerol, T. Siemieniewska, Pure Appl. Chem. 57 (1985) 603–619.
[31] J. Yoo, R. Araujo, N. Grunbaum, L. Baqué, A. Serquis, A. Caneiro, X. Zhang, H. Wang, Appl. Surf. Sci 254 (2007) 266–269.
[32] D.Z. De Florio, R. Muccillo, V. Esposito, E. Di Bartolomeo, E. Traversa, J. Electrochem. Soc. 152 (2005) A88–A92.
[33] S.B. Adler, Solid State Ionics 111 (1998) 125–134.
[34] Y. Takeda, R. Kanno, M. Noda, Y. Tomida, O. Yamamoto, J. Electrochem. Soc. 134 (1987) 2656–2661.
[35] A. Ringuedé, J. Fouletier, Solid State Ionics 139 (2001) 168–177.
[36] T. Kawada, J. Suzuki, M. Sase, A. Kaimai, Y. Nigara, J. Mizusaki, K. Kawamura, H. Yugami, J. Electrochem. Soc. 149 (2002) E252–E259.
[37] N. Grunbaum, L. Dessemond, J. Fouletier, F. Prado, L. Mogni, A. Caneiro, Solid State Ionics 180 (2009) 1448–1452.
[38] S. Wang, J. Yoon, G. Kim, D. Huang, H. Wang, A.J. Jacobson, Chem. Mater. 22 (2010) 776–782.
[39] L.M.P. García, D.A. Macedo, G.L. Souza, F.V. Motta, C.A. Paskocimas, R.M. Nascimento, Ceram. Inter. 39 (2013) 8385–8392.

[40] S.B. Adler, J.A. Lane, B.C.H. Steele, J. Electrochem. Soc. 143 (1996) 3554–3564.
[41] X.J. Chen, S.H. Chan, K.A. Khor, Electrochim. Acta 49 (2004) 1851–1861.
[42] D. Marrero-López, R. Romero, F. Martín, J.R. Ramos-Barrado, J. Power Sources 255 (2014) 308–317.
[43] D. Marinha, L. Dessemond, J.S. Cronin, J.R. Wilson, S.A. Barnett, E. Djurado, Chem. Mater. 23 (2011) 5340–5348.
[44] F.S. Baumann, J. Fleig, H.-U. Habermeier, J. Maier, Solid State Ionics 177 (2006) 1071–1081.
[45] D. Marinha, L. Dessemond, E. Djurado, J. Power Sources 197 (2012) 80–87.
[46] A. Ringuedé, J. Fouletier, Solid. State Ionics 139 (2001) 167–177.
[47] F. Baumann, J. Fleig, H.-U. Habermeier, J. Maier, Solid State Ionics 177 (2006) 3187–3191.
[48] A. Endo, H. Fukunaga, C. Wen, K. Yamada, Solid State Ionics 135 (2000) 353–358.
[49] D. Florio, R. Muccillo, V. Esposito, E. Di Bartolomeo, E. Traversa, J. Electrochem. Soc. 152 (2005) A88–A92.
[50] H. Fukunaga, M. Koyama, N. Takahashi, C. Wen, K. Yamada, Solid State Ionics 132 (2000) 279–285.
[51] S. Adler, Chem. Rev. 104 (2004) 4791–4843.
[52] J. Fleig, J. Maier, J. Eur. Ceram. Soc. 24 (2004) 1343–1347.
[53] W. Guo, J. Liu, C. Jin, H. Gao, Y. Zhang, J. Alloys Compd. 473 (2009) 43–47.
[54] L. Baqué, A. Caneiro, M.S. Moreno, A. Serquis, Electrochem. Comm. 10 (2008) 1905–1908.